energy&fuels

pubs.acs.org/EF

Article

Phase Transitions and Separation Time Scales of CO_2–Crude Oil Fluid Systems: Wheel Flow Loop Experiments and Modeling

Martin Fossen,*[,§] Marcelo A. Pasqualette,[§] and João N. E. Carneiro[§]

Cite This: https://dx.doi.org/10.1021/acs.energyfuels.0c00818

Read Online

ACCESS | Metrics & More | Article Recommendations

ABSTRACT: Presented here is experimental and theoretical work on phase transitions and separation time scales for CO_2–crude oil mixtures with CO_2 content ranging from pure to 79 mol %. The experimental work was performed using the wheel flow loop located at the SINTEF Multiphase Flow Laboratory. Under constant volume conditions, phase transition temperature and pressures were determined, as well as the volume fractions of the respective phases. The results indicated good agreement between the experimentally determined phase transitions and the phase diagrams predicted by the thermodynamic model. It was shown that the measured torque was sufficient to determine the pressure–temperature conditions of the phase transitions. Furthermore, separation times were measured for both oil-in-CO_2 and CO_2-in-oil in a range of conditions for the respective fluid systems. Results showed that the separation times were considerably shorter for the CO_2 continuous fluid system compared to oil continuous. Moreover, a comparison of Weber numbers for the various test conditions indicated that the drop sizes influence the overall separation time, which is affected by settling and coalescence processes. Finally, this study showed that the wheel flow loop is well suited for the study of CO_2-rich systems for determination of volume fractions of phases, phase transitions, and transport and separation.

1. INTRODUCTION

1.1. CO_2 Rich Oil and Gas Fields. The transport of CO_2-rich fluids through pipelines has become increasingly relevant due to increased focus on carbon capture and storage (CCS) technologies and enhanced oil recovery (EOR) by CO_2 flooding.[1] In oil and gas fields where CO_2-rich gas reinjection (for storage and/or CO_2 flooding purposes) takes place, back production of CO_2 increases its content in the well stream. Regarding EOR, some examples of CO_2 flooding projects include the Permian Basin onshore area in the United States and the Bati Raman field in Turkey.[2] Furthermore, CO_2 can be directly available from associated gas during production such as for the presalt reservoirs in the Santos Basin in Brazil[3,4] and in the Neuquen province in central Argentina, which contains as much as 45–75 mol % CO_2 in the produced gas.[5,6] In some Brazilian presalt fields, the approximate CO_2 molar fractions are 17.5% (associated gas) in the Sapinhoá field,[7] 44 mol % (associated gas) in the Libra field,[8] and 55 mol % (oil) and 79 mol % (gas cap) in the Júpiter field.[9] Reinjection of CO_2 for EOR is considered attractive for some Brazilian presalt fields[4] but is expected to increase the CO_2 concentration and GOR in production fluids in the future.[10]

1.2. Some Challenges Related to CO_2 Rich Fluids. CO_2–crude oil systems may show complex phase behaviors[2,11,12] and can result in systems containing multiple phases depending on the fluid mixture and pressure and temperature conditions. For nonaqueous mixtures, at temperatures much higher than the CO_2 critical temperature, CO_2 and crude oil forms up to two phases.[2] For lower temperatures, either two or three phases are possible. For high CO_2 fractions, typically above 50–60 mol % at higher pressures, a heavier hydrocarbon-rich liquid may coexist with a CO_2-rich liquid phase.[2,12]

If, during a sweep process, a CO_2-rich front breaks through and reaches the production well, the CO_2 content in the production stream will increase significantly, indicating the importance of predictability of CO_2-rich systems.[13−16] Nonetheless, the validity of mechanistic models may be questioned if CO_2-rich dense phases are not treated appropriately.[16] Furthermore, CO_2-rich hydrocarbon mixtures raise pipeline integrity and flow assurance concerns due to potential asphaltene precipitation,[17,18] corrosion challenges,[19] swelling of the polymeric liners,[20] and calcium carbonate scaling.[21] In addition, supercritical CO_2 has strong solvent/extraction properties[22] and may damage plasticized polymers. If water is present under low temperatures and high pressures, the possibility of formation of CO_2 hydrates is another challenge that needs to be tackled.[23]

1.3. Separation of CO_2–Oil Systems. In some Brazilian presalt areas, the possibility of separating a dense CO_2-rich phase at the seabed is under investigation.[24] An example is the "HiSep" technology,[25] where the aim is to compress the high-density CO_2-rich phase back into the reservoir, thus alleviating the processing requirements topside. Some experimental studies have been performed under static conditions,[12,26,27] but a more detailed understanding of such systems across a range of compositions and thermodynamic states is needed.

Received: March 15, 2020
Revised: May 12, 2020
Published: May 13, 2020

According to Alzobaidi et al.,[28] only a few studies have looked at stabilization of CO_2−oil dispersions, as it is not expected that there are surfactants that can stabilize that interface. Under that assumption, the dispersion stability should mainly be a function of droplet size, surface tension, relative density between the two liquid phases, and the oil viscosity.

1.4. Aim and Motivation. Herein, we aim to describe phase transitions, phase fraction volumes, and separation time scales of some selected fluid mixtures containing CO_2, mineral oil, crude oil, and small amounts of methane. The mixture of mineral oil and crude oil was selected to make a test case with a model crude oil system. While a light low molecular weight oil only forms a liquid−gas system with CO_2, the more complex mineral oil−crude oil mixture forms a three-phase liquid−liquid−gas with CO_2 at lower pressures and temperatures, and two phases at higher pressures and temperatures. Thus, the motivation for this study was to get experimental data on phase fractions and separation time scales of liquid or dense phase CO_2−oil mixtures for systems containing various amounts of CO_2. By using a wheel shaped flow loop (the wheel), which is a closed system, it was possible to achieve phase transition by adjusting the temperature only. Use of the wheel has previously been reported in the literature by several authors.[29−32] The results of the current work presented here indicated that, in general, the thermodynamic models were appropriate for the current system. Furthermore, the separation studies indicated that, for the design and operation of CO_2−oil separation units and transport of CO_2 rich fluids, it is important to be able to predict which liquid phase is the continuous one and the separation time scale expected for a given fluid system under operating conditions.

2. MATERIALS AND METHODS

2.1. Materials. The fluid systems used were comprised of mixtures containing carbon dioxide (CO_2) from VWR with a purity of 99.7%; Exxsol D80 (mineral oil) from ExxonMobile Petroleum and Chemical BVBA/Esso Norge, which is a dearomatized (<2% aromatics) hydrocarbon liquid consisting of C11−C14 *n*-alkanes, iso-alkanes, and cyclic components (ExxonMobil Materials Safety Data Sheet 3.10); an anonymized crude oil; and Chemical Methane 2.5 (CH_4) from VWR. Key data on the mineral oil and crude oil are given in Table 1 below.

The crude oil sample was chosen from available samples located at the SINTEF lab and mixed with the mineral oil in order to not represent any specific crude oil, but rather an exemplified crude oil system which be considered as a model system for a crude oil. The crude oil used was a relatively light oil (838 kg/m^3), with negligible asphaltene content. The wax content was 6.6 wt %, and the total acid number (TAN) was less than 0.1 mg KOH/g. The chemical composition of the crude oil is more complex containing larger molecules enabling the formation of three-phase systems at appropriate pressure−temperature conditions. Thus, the mineral oil−crude oil mixture would behave thermodynamically like a typical relatively light crude oil.

Table 1. Key Available Data on the Crude and Mineral Oils

crude oil		Exxsol D80	
parameter	reference	parameter	datasheets
molar mass	183.26 g/mol	carbon numbers	11−14
density @ 15.6 °C, 1 atm	838 kg/m^3	aromatic content	0.2−0.3 wt %
dynamic viscosity @ 15.6 °C, 1 atm	5.0 mPa·s	vapor pressure @ 20 °C	10.0−13.3 Pa
saturates	74.6 wt %	density @ 15.6 °C, 1 atm	794−796 kg/m^3
aromatics	21.1 wt %	kinematic viscosity @ 25 °C, 1 atm	1.7 mPa·s
polar (resins)	4.3 wt %		
asphaltenes	0.0 wt %		
wax (purified)	6.6 wt %		
TAN	<0.1 mg KOH/g		

2.2. Methods. *2.2.1. Experimental Setup: The Wheel Flow Loop.* The experimental set up used for the current tests consisted of the wheel located at SINTEF's Multiphase Flow Facility at Tiller, Trondheim in Norway. It is a closed system, consisting of two 2″ (inner diameter of 52.5 mm and wall thickness of 3.91 mm) duplex steel pipes bent into semicircular shapes and mounted together to form a circle ("wheel shaped") with a diameter of 2 m and circumference of 6.28 m, giving a total volume inside of 13.4 L. The two semicircles were connected with a short steel pipe spacer at one side and a sapphire pipe section for visual observations on the other side. A picture of the actual wheel is given in Figure 1a and in addition two illustrations, one indicating the main features of the wheel (Figure 1b) and the other (Figure 1c) an illustration for the explanation of how phase fractions were determined as described below. When partially filled with liquid, the heaviest phase would be located in the lower section as indicated by the oil−gas interface in Figure 1b. If three phases were present, the lowest density fluid (typically the gas phase) would be located in the upper part of the wheel, while the intermediate density (liquid) phase would occupy the volumes between the upper and lower parts of the wheel and the heaviest liquid phase would be located at the bottom as indicated in Figure 1c. The wheel was positioned vertically and attached to a shaft and a motor to enable rotation at velocities (stagnant liquid relative to the pipe wall) up to 5 m/s. The motor had a position indicator outputting the angle, 0−360°, which was used to determine the position of interfaces by placing the optical window at their location. Furthermore, when rotating the wheel, the fluids inside experience a shear force, enabling the formation of both gas−liquid and liquid−liquid dispersions. A torque sensor on the shaft was used to measure changes in the overall shear force while rotating and was used to determine phase transition points as described in more detail below. One of the main advantages of the wheel is the possibility to keep the pipe flow conditions for a long duration of time without the need for pumps, compressors, or separators. Furthermore, the wheel was placed in a temperature-controlled chamber allowing the fluids to be heated or cooled at defined rates. The application of a wheel shaped flow loop concept was reported as early as 1971.[33] The wheel apparatus has been used for measuring emulsion viscosity under flowing conditions through torque measurements[29−32] and for hydrate slurry transport studies.[34]

2.2.2. Filling Procedure and Determination of the Phase Fractions in the Wheel. The wheel was filled by pumping the appropriate liquids and gases separately using high pressure pumps/compressors. The wheel rested on a weight, and all fluids (liquids and gases) were filled on a weight basis. Successive filling was performed in this study. At first, CO_2 was filled stepwise, followed by the oils in several steps and, finally, for the last fluid system, a small amount of methane. For each filling step, the new composition was given a number: "Fluid System 1" (FS1), "Fluid System 2" (FS2), and so on. For each fluid system, the accumulated amount (in kg mass) of each component (CO_2, mineral oil, crude oil, and methane), the observed phases for the range of pressure−temperature (P−T) conditions, and the mole fraction of CO_2 are shown in Figure 3.

2.2.3. Determination of Phase Transitions. For each fluid system, temperature was varied to identify possible phase transitions and determine the nature and relative amounts of each phase at the relevant conditions. For selected fluid systems, separation times for dispersions were determined experimentally. The phase transitions were determined by rotating the wheel at a constant velocity while changing the temperature until the phase boundary was crossed. Under constant velocity the friction between the fluids inside the

https://dx.doi.org/10.1021/acs.energyfuels.0c00818
Energy Fuels XXXX, XXX, XXX−XXX

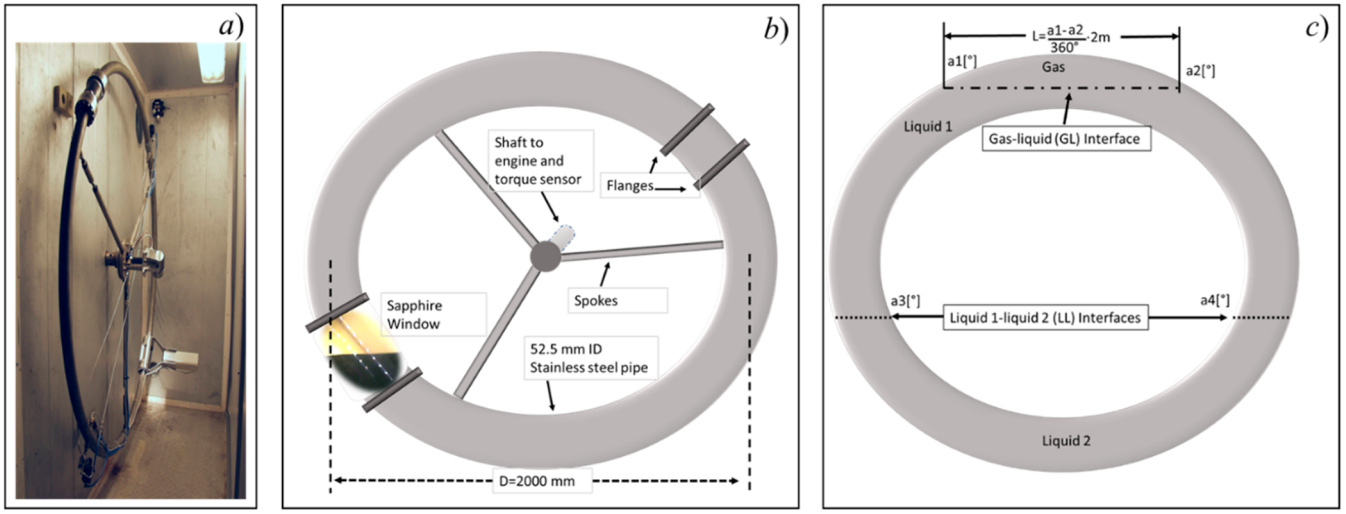

Figure 1. (a) Picture of the wheel. (b) Schematic illustration with main details indicated. (c) How the location of the interfaces were used to determine the relative volume fractions of the phases present in the wheel.

wheel and the pipe wall will vary depending on the nature and relative volume fractions of phases inside the wheel. Thus, by keeping a constant velocity while changing the temperature, the measured torque values would change significantly, and this was used as an indirect method to determine the pressure and temperature of the phase transitions. Moreover, the volumes of each phase were determined by visual inspection. This was done by identifying the position (angle) of each interface while the wheel was stagnant. Then the ratio of the measured coverage in terms of angular degrees to the total angular degrees (360°) was multiplied with the total length, L (circumference), of the wheel. This length was then used to calculate the volume of the respective phase fractions. The determination of the phase fraction in the wheel is illustrated by Figure 1c, indicating a three-phase gas−liquid−liquid system (GLL). The gas−liquid interface is positioned in the upper part of the wheel (as indicated). The GL interface is spanning the length indicated by the two measured angles, a1 and a2, from which the length and thus the volume of the gas phase can be determined as described above. Furthermore, the measured angles a3 and a4 were used to determine the volume of the liquid phase at the bottom of the wheel, here called liquid 2. Thus, the other liquid phase (liquid 1) occupies the remaining volume of the wheel.

An evaluation on the possible error of the above method for determining the volumes was done by comparing with volumes calculated using an expression for a toroid. It was found that for the majority of cases, direct calculation of the volumes by the method described above was adequate. However, for cases where the volume of the lowest or highest density phase was very low (top or bottom of the wheel), as exemplified with the gas phase in Figure 1c, the toroid approach resulted in values of up to 8% higher phase fraction and would be more correct, as it captures the effect of the curvature of the pipe. Furthermore, the total angle covered by the window sections was 7°. If allowing an uncertainty of 1° (equivalent to 1.5 cm) at each side of a given measured interface (perpendicular to the pipe wall), the maximum uncertainty in terms of volumes would be 74 mL.

2.2.4. Thermodynamic Modeling. KBC/Infochem Multiflash v7.0.4 (January/2019; Multiflash) with the Cubic Plus Associating (CPA) Equation of State (EOS)[35] was used to predict the phase diagrams and fluid properties. For CO_2-rich oil mixtures, this EOS should perform better than standard cubic EOSs, such as Peng−Robinson[36] and Soave−Redlich−Kwong[37] with Péneloux-like[38] volume corrections.[39] Despite that it does not explicitly account for the strong quadrupolar moment of the CO_2, which could enhance the performance of associating EOS,[40,41] the CPA EOS version implemented in the thermodynamic software was deemed accurate enough for comparison with the experimental data. The fluid systems 1 to 5 (only CO_2) were satisfactorily modeled. The mineral oil composition was created using hydrocarbon pseudocomponents with carbon numbers of 11, 12, 13, and 14 at equal mass fractions. The properties (such as critical temperature, pressure, and acentric factor) of these pseudocomponents were estimated with Multiflash internal correlations.[42,43] Moreover, the thermodynamic model was complemented by the Pedersen viscosity model,[44,45] and density and viscosity estimates were created (Table 2) and compared with the datasheet reference data from Table 1. Furthermore, the comparison indicated that the model was valid for this fluid.

Table 2. Evaluation on the Thermodynamic Numerical Predictions against the Reference Data

oil	parameter	numerical	error (vs reference data)
Exxsol D80	density @ 15.6 °C, 1 atm	810 kg/m^3	1.8%
Exxsol D80	kinematic Viscosity @ 25 °C, 1 atm	2.23 mm^2/s	1.9%
crude oil	density @ 15.6 °C, 1 atm	835 kg/m^3	−0.4%
crude oil	dynamic viscosity @ 15.6 °C, 1 atm	5.0 mPa·s	0%

The characterized crude oil composition, based on gas chromatography data, was available (Figure 2). Moreover, the unknown properties of the pseudocomponents of the crude oil were evaluated by the Multiflash internal correlations.[42,43] Once again, density and viscosity calculations were performed (Table 2) and compared against the reference data from Table 1. Without calibration, the model predicted satisfactorily the density and dynamic viscosity of the crude oil and was deemed appropriate for the current study.

From compositional data in Figure 3 and with the temperature and pressure data from the experiments, it was possible to compare the experimentally determined phases with the phase diagrams of each fluid system. Thus, by mixing the mass fractions of the respective fluid systems given in Figure 3, the phase diagrams were predicted and compared with the experimental observations. Such phase diagrams were built with a combination of the Multiflash Excel add-in and in-house VBA and Python scripts.

2.2.5. Estimation of Settling and Coalescence Time Scales. The CO_2−oil dispersions were formed by shear forces due to friction between pipe wall and fluids upon rotation. When stopping the rotation and positioning the $CO_{2(l)}$−oil or $CO_{2(dp)}$−oil interface (l being liquid phase and dp being the CO_2 dense phase) to be observed through the sapphire window, the separation was monitored and

https://dx.doi.org/10.1021/acs.energyfuels.0c00818
Energy Fuels XXXX, XXX, XXX−XXX

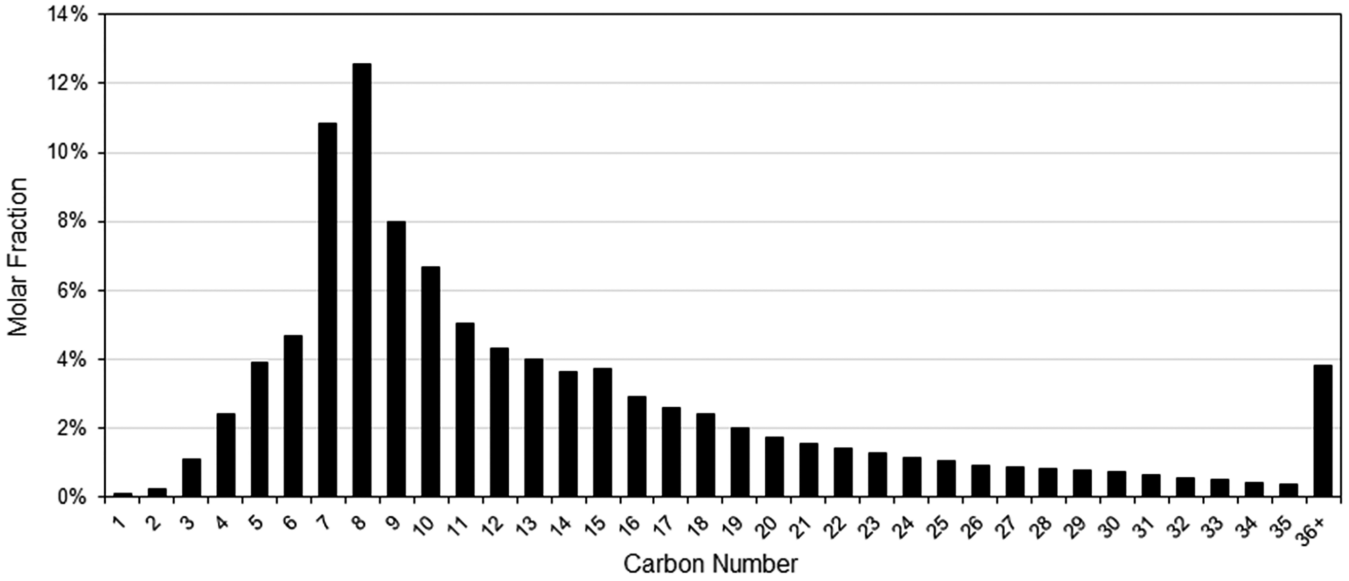

Figure 2. Carbon number distribution (molar fractions) of the crude oil.

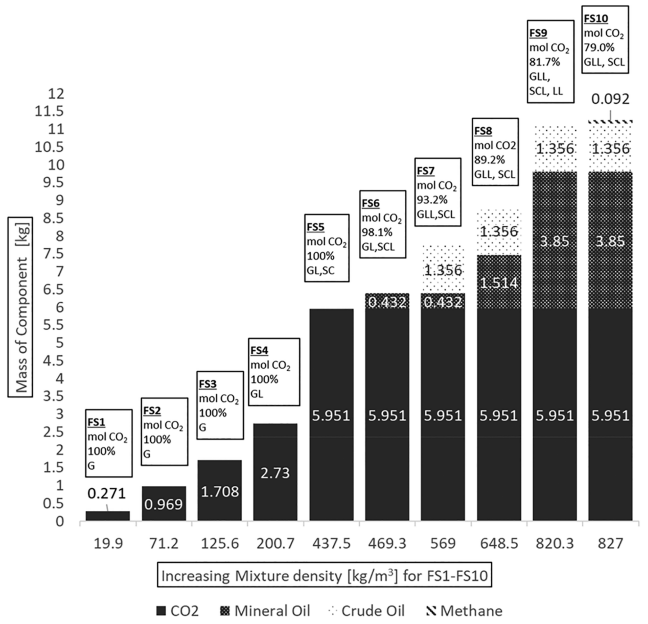

Figure 3. Graphical representation of the amounts (kg) of each phase (CO_2, mineral oil, crude oil, and methane) in the wheel for each fluid system (FS1−10). Information on the mixture densities (total mass divided by total wheel volume) are found along the *x*-axis, and the amounts in kilograms filled are represented in the bar plots. Text boxes above each bar plot provide the mole fraction of CO_2, and phases observed are shortened as G (gas CO_2), GL_{CO2} (gas CO_2−liquid CO_2), GL_{oil} (gas CO_2−liquid oil), SC (supercritical CO_2), SCL (supercritical CO_2 + liquid oil), GLL (gas CO_2−liquid CO_2−liquid oil), and LL (liquid CO_2−liquid oil).

recorded for post-determination of separation times. The measured time duration data were then compared to both a simple correlation (τ_{corr}) and to separate expressions for settling (τ_s) and coalescence (τ_c) times, which, when summed, result in the separation time.

The simplified correlation for the separation time scale that was developed is given by eq 1:

$$\tau_{corr}[\text{min}] = \kappa_0 \left(\frac{\mu_c}{\mu_d}\right)^{\kappa_1} (\text{Eo}_p)^{\kappa_2} \quad (1)$$

where Eo_p is the Eötvös number, μ_c and μ_d are the dynamic viscosities of the continuous and dispersed phases, respectively, and the constants κ_0, κ_1, and κ_2 were obtained by tuning with the available experimental data. In the above equation, $\text{Eo}_p = |\Delta\rho| g d_{pipe}/\sigma$ is a function of the pipe internal diameter d_{pipe}, the density difference $\Delta\rho$ of the two liquids, the gravitational constant g, and the interfacial tension σ between the two liquids. A high value of Eo_p suggests a large driving force for separation (due to high density difference between the phases), in relation to surface tension forces.[46] Furthermore, according to Calabrese et al.,[47] the dispersed phase viscosity may also have a relevant effect because the internal stresses influence the drop deformability.

For more detailed analysis of the separation process, the separation was divided into a settling (τ_s) and a coalescence (τ_c) part, each with its own expression. The settling (or rise) time scale τ_s of the droplets in a swarm of droplets may be directly calculated by eq 2:

$$\tau_s[\text{min}] = \frac{L_c}{60 V_T} \quad (2)$$

where L_c is a characteristic distance traveled by the droplets. Due to the curved geometry of the wheel and the dynamic nature of the process (the interface moves as the separation progresses), the expression in eq 3 was used to describe L_c as a power law depending on the continuous liquid volume fraction α_c and the total emulsion volume fraction $\alpha_{em} = \alpha_d + \alpha_c$ (α_d is the dispersed liquid volume fraction) in the wheel:

$$L_c = C_0 (\alpha_c)^{C_1} (\alpha_{em})^{C_2} \quad (3)$$

where the values of the constants C_1 and C_2 were fitted to experimental data (as shown below). The velocity V_T can, for dense dispersions, be described with the expression of Kumar and Hartland,[48] provided in eq 4:

$$V_T = \frac{\mu_c}{\rho_c d_{32}} \left\{ -\frac{12}{\varphi_1} + \sqrt{\left(\frac{12}{\varphi_1}\right)^2 + \frac{4}{3\varphi_1}\left[\frac{1-\alpha_d^*}{1+\varphi_2(\alpha_d^*)^{\varphi_3}}\right]\text{Ar}} \right\} \quad (4)$$

where ρ_c is the density of the continuous liquid phase, d_{32} is the Sauter mean diameter of the dispersed liquid phase; $\alpha_d^* = \alpha_d/\alpha_{em}$ is the dispersed liquid phase volume fraction in relation to the emulsion volume; $\text{Ar} = g\rho_c|\Delta\rho|(d_{32})^3/\mu_c^2$ is the Archimedes number; and φ_1 =

https://dx.doi.org/10.1021/acs.energyfuels.0c00818
Energy Fuels XXXX, XXX, XXX−XXX

0.53, φ_2 = 4.56, and φ_3 = 0.73 are empirical coefficients determined by Kumar and Hartland.[48]

For the determination of d_{32}, an expression, eq 5, that takes into account the dispersed phase volume fractions was used:[49]

$$\frac{d_{32}}{D_W} = 0.083(1 + 4\alpha_d^*)^{1.2}\mathrm{We}^{-0.6} \quad (5)$$

where D_W is the wheel total diameter (2 m, for the present experimental setup) and $\mathrm{We} = \rho_c U_W^2 d_{pipe}/\sigma$ is a Weber number, expressed as a function of the wheel velocity U_W, among other parameters.

During the separation of the oil and CO_2 phase (liquid or dense phase), drops coalesce with themselves and with the interface of their homophase.[50] Coalescence phenomena are complex and difficult to characterize experimentally and a general modeling framework for droplet lifetimes incorporating droplet diameter, fluid properties, and surfactants does not appear to be well established. Nevertheless, the possibility of representing the resting (or coalescence) time of droplets (τ_c) at a flat interface as a power law correlation with the drop diameter has been determined experimentally:[51] $\tau_c \sim (d_{32})^{\chi}$ (χ is an experimentally determined power law exponent). The exponent χ, for a given physical system, is found by controlling the initial drop sizes and measuring the drop coalescence time. According to Kamp et al.,[52] the values of χ may vary significantly depending on the fluid system and the range of drop sizes investigated. Furthermore, Basheva et al.[53] observed that the dependency of drop size on the coalescence time is strong and that a transition from small rigid droplets (<20 μm) to bigger deformable drops can be observed in the same physical system, giving significant variations in the power law exponent χ.

According to the conceptual models of Hartland and Jeelani[54] for a batch sedimentation setup with concentrated dispersions, droplets first settle to form a dense packed layer. This layer tends to increase up to a point where droplets coalesce with its homophase followed by a decrease in the dense packed layer until complete phase separation. For the drop−drop coalescence process at a dense packed layer, Jeffreys et al.[55] and, according to Jaradat et al.,[56] Henschke in his Ph.D. dissertation,[57] determined that the time scale for coalescence may also be determined by a power law of the form $\tau_c \sim (d_{32})^{\chi}$, as for the drop rest time at a flat interface, as discussed above.

Therefore, in order to perform a time scale analysis for comparisons with the sedimentation time τ_s, an overall coalescence time scale τ_c was developed here, in eq 6:

$$\tau_c[\mathrm{min}] = \chi_0\left(\frac{\mu_c}{\mu_d}\right)^{\chi_1}(\mathrm{Eo}_p)^{\chi_2}\left(\frac{d_{32}}{D_W}\right)^{\chi_3} \quad (6)$$

where χ_0, χ_1, χ_2, and χ_3 are fitting parameters. Note that the first terms of the equation are similar to the simplified time scale correlation, τ_{corr}, eq 1, while the last term incorporates the dependency with the Sauter mean diameter.

3. RESULTS AND DISCUSSION

3.1. Measured Phase Fractions at Specific Pressure−Temperature Points. The accumulated masses of each component for the fluid systems, as well as the mixture densities, the mol % of CO_2, and the phases observed (for relevant temperature range tested) are provided in Figure 3.

The measured relative phase fraction volumes for specific temperature−pressure conditions are given in Figure 4 for the fluid systems 4 and 5 and 7−10. The FS6 consisted of CO_2 and mineral oil and formed a two-phase GL system below the critical point for CO_2 and a single phase and SCL (supercritical CO_2 + liquid oil) system above such a critical point. However, the relative phase fractions were not measured for this system, which is why it is not included in Figure 4. For FS8, the oil phase volume increased at the expense of the liquid CO_2 phase up to 44 °C and 83 bar, while at 44 °C and 87 bar the FS8 system had undergone phase transition into a two phase supercritical (dense phase) CO_2 and the oil phase. A similar observation was made for FS9, also seen in Figure 4. Thus, the results indicate the solubility of CO_2 in the oil phase and the effect of changing the temperature under the test conditions. Furthermore, the experimentally determined phases were compared with the phase diagrams predicted by the thermodynamic model (Figures 6 and 7).

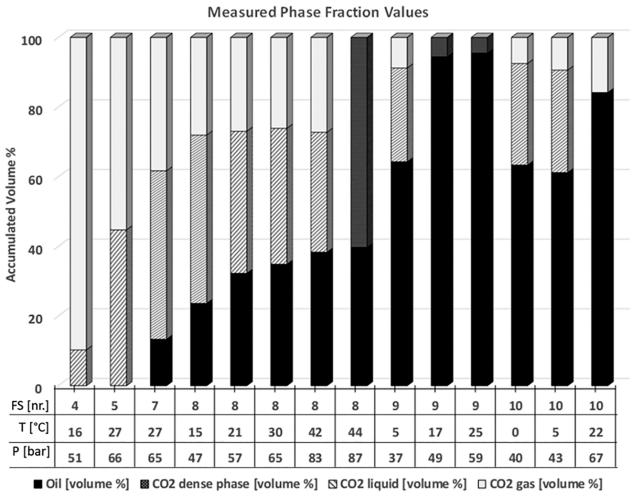

Figure 4. A graphical representation of the measured phase volume fractions at selected pressure−temperature points for FS4 and 5 and 7−10.

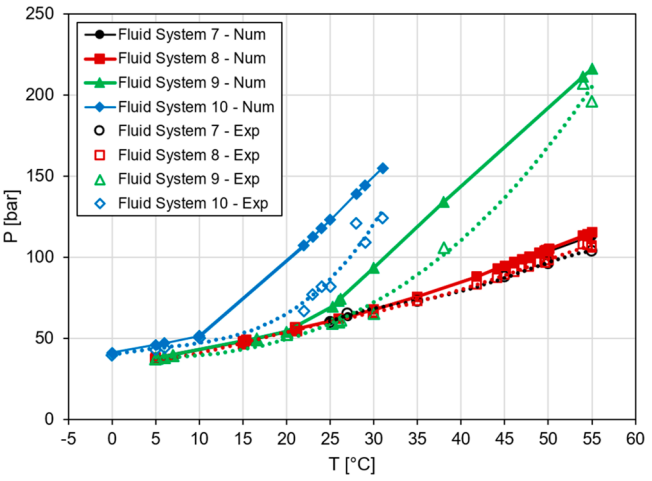

Figure 5. Comparison between experimental and numerical $T-P$ isopleths for fluid systems 7−10 (the dashed lines correspond to fitting of the experimental data).

3.2. Evaluation of the Thermodynamic Model. The numerical and experimental temperature−pressure ($T-P$) isopleths of constant mixture densities for fluid systems 7−10 are compared in Figure 5, revealing good agreement of the thermodynamic model for FS7 and FS8 with the experimental data. For systems FS9 (which had a much higher oil content) and FS10 (addition of a small amount of methane) the deviations were larger, consistent with results reported previously for similar systems.[12] Furthermore, the predictions showed that FS9 obtained a much more complex phase behavior than for the lower mixture densities (FS7 and FS8) and further that a small amount (92 g) of methane changed the

https://dx.doi.org/10.1021/acs.energyfuels.0c00818
Energy Fuels XXXX, XXX, XXX−XXX

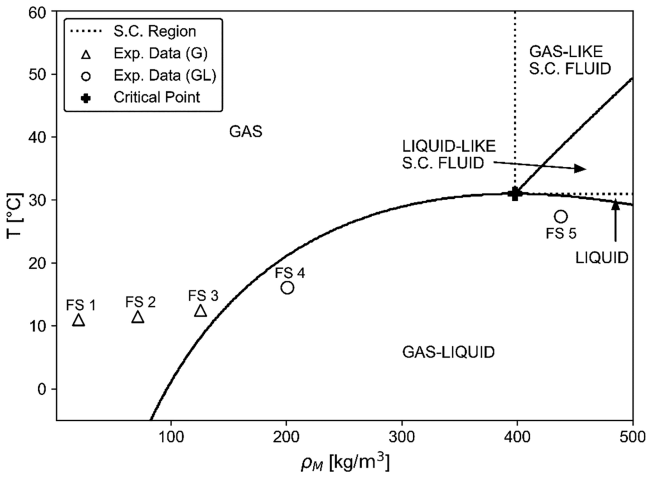

Figure 6. Predicted $T-\rho$ phase diagram for single component CO_2 and the phase behavior equilibria observations for fluid systems (mixture densities ρ_M) 1−5 represented by the triangles (FS1−3) and circles (FS4 and 5).

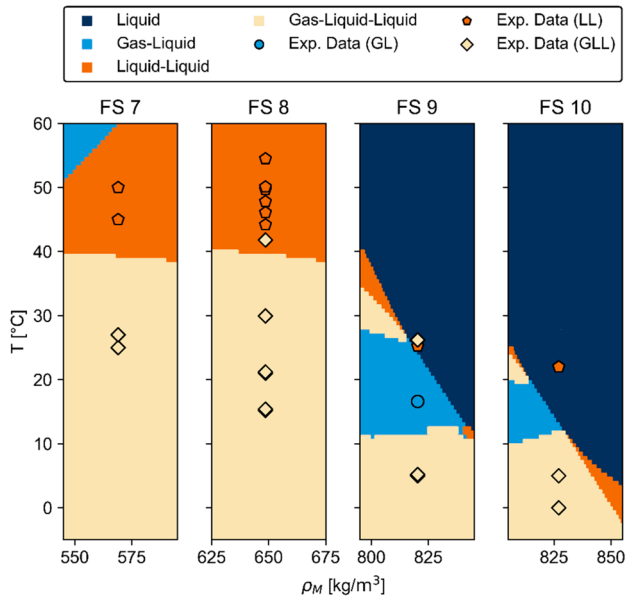

Figure 7. Predicted temperature−mixture density (T vs ρ_M) phase diagrams and the phase equilibria observations for fluid systems (FS) 7−10.

phase diagram significantly as seen when comparing the phase diagrams of FS8 with FS9 and FS9 with FS10 in Figure 7.

3.3. Comparison of Phase Diagrams with Experimental Observations. The observed phases are plotted in the temperature−density ($T-\rho$) phase diagram for pure CO_2 for fluid systems 1−5 (Figure 6) and indicate the change from a single to a two-phase system for increasing mixture density (ρ_M). The choice of representing the system in $T-\rho$ was because in a $T-P$ phase diagram the two-phase region would only be a line, according to the Gibbs phase rule[58] and the three-phase regions in similar diagrams for CO_2-rich oil mixtures are also expected to be very narrow.[12,26,27] Thus, the $T-\rho$ diagram makes the numerical−experimental comparison easier to follow since the two- and three-phase regions are wider compared to a temperature−pressure phase diagram. In Figure 6, the supercritical (SC) region is highlighted as well as its gas-like and liquid-like regions, which are divided according to the critical properties-based phase identification criteria of Multiflash. The phase diagrams for fluid systems 7−10 are provided in Figure 7, with indication of the experimentally observed phases and how they compare with the predicted phases for respective $T-\rho$ combinations. Furthermore, in the plots indicating phase transitions determined from wheel tests (Figures 8−12), the $T-\rho$ locations in the phase diagrams are indicated together with the pressure, temperature, and torque profiles.

3.4. Experimental Determination of Phase Transition Conditions. As explained above, the phase transitions were determined by distinct changes in the torque values when simultaneously rotating the wheel at a constant velocity while changing the temperature. For fluid system FS7 the wheel was rotated at 1.5 m/s while being heated from 35 to 54 °C at 0.13 °C/min. The torque data indicated (by a sudden drop) phase transition at 42.7 °C and 84.5 bar with the three-phase system below and the two-phase (supercritical CO_2 and oil) above this $T-P$ point as indicated in Figure 8. In comparison, the predicted phase transitions occurred at 38.9 °C and 82.0 bar as indicated by the phase diagram for FS7 in the same figure. The location of the experimental values (in terms of the temperature) is indicated in the phase diagrams (Figure 7), while Table 3 provides a summary of the phase transition points (P and T) given in the plots for the fluid systems FS7−FS10 below (Figures 8−12).

Fluid system FS8 experienced the phase transition from three-phase GLL to two-phase LL at 44.1 °C and 87 bar (Figure 9), while the predicted phase transition point was 39.3 °C and 82.8 bar. The rotational velocity used in this test was 1 m/s, and the temperature increased at a rate of ∼0.1 °C around the point of the phase transition.

Fluid system FS9, after the addition of 2300 g of mineral oil, experienced two phase transitions (and three different regions of the phase diagram) as indicated from the torque data in Figure 10 (decreasing from 0.1 N m to 1.5 N m). Upon heating the system at a rate of 0.26 °C, while rotating at a constant velocity of 1 m/s, the results showed that below 18.7 °C and 50.6 bar, a three-phase GLL and, above 32.7 °C and 68.2 bar, a single liquid (L) phase existed (the phases were determined by visual observations as explained elsewhere). Between these two regions, a two-phase GL system existed. The observed transitions corresponded with the phases predicted by the EOS, also seen in Figure 10. By moving in the opposite direction (temperature wise) through the phase diagram, by cooling at 0.2 °C/min, phase transition from the single liquid phase started at 30.5 °C and 66.1 bar and ended at 17.3 °C and 49.8 bar (Figure 11). The reason for the apparent deviation in phase transition points when heating versus cooling the system was not studied further but should be in future studies by attempting lower heating and cooling rates. The continuous change in torque observed between ∼32 °C and ∼17 °C for both cooling and heating of the system at constant rotational velocity was most probably due to continuous changes in the gas−liquid ratio and thus the shear force of the system.

The presence of the observed transition region of the two-phase GL conditions may be of importance for understanding and predicting pressure drop along transport pipelines where the conditions (pressure, temperature and density) can change considerably. Furthermore, the knowledge and ability to predict the pressure drops based on the phase conditions

https://dx.doi.org/10.1021/acs.energyfuels.0c00818
Energy Fuels XXXX, XXX, XXX−XXX

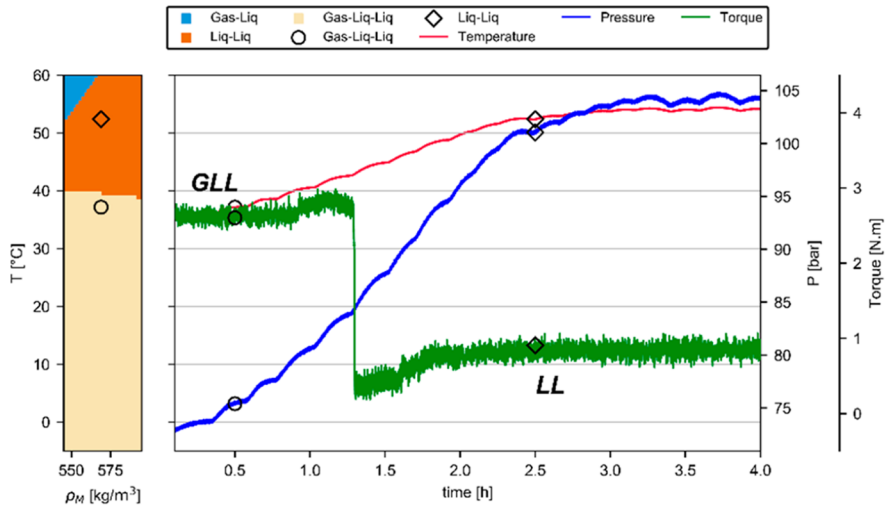

Figure 8. Results from phase transition data for FS7. Torque values (green line) dropped as temperature (red line) was increased, indicating phase transition. To the left is the phase diagram predicted for FS7. The wheel was rotated at 1.5 m/s while heating across the GLL/LL phase boundary. Indicated on the plot are the GLL and the LL phases.

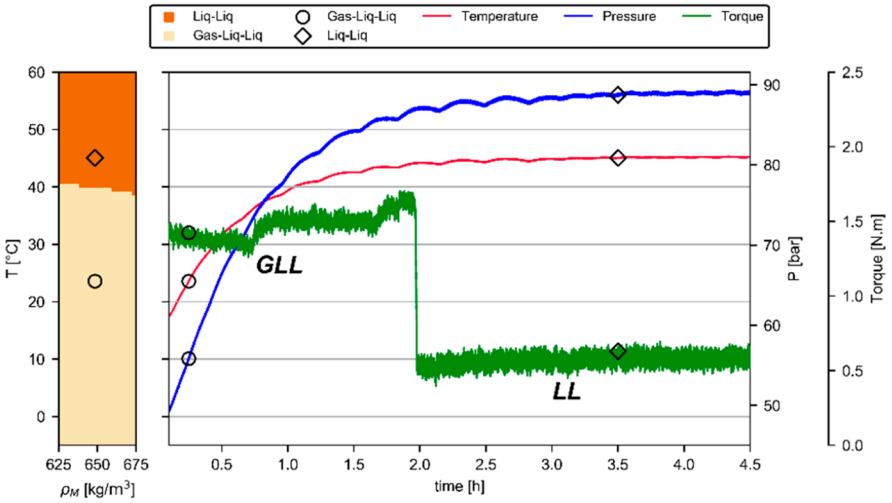

Figure 9. Results from phase transition data for FS8. Torque values (green line) dropped as temperature (red line) was increased, indicating phase transition. To the left is the phase diagram predicted for FS8. The wheel was rotated at 1.0 m/s while heating across the GLL/LL phase boundary. Indicated on the plot are the GLL and the LL phases.

will be important for optimizing transport and flow assurance when producing rich CO_2−oil systems and for CCS applications.

For FS10, an additional amount of 92 g of methane was filled to FS9. The phase transition was studied by cooling the system from 32 to 5 °C, at a rate of 0.2 °C/min while rotating the wheel at 0.5 m/s. Only one phase transition was observed from LL (liquid oil and liquid CO_2) to GLL (gas CO_2, liquid CO_2 and liquid oil), starting at 19.5 °C and 61.9 bar ending at 18.9 °C and 61 bar. Furthermore, for FS10, the density of the CO_2 phase became heavier than the density of the oil phase, below 12 °C and 51.2 bar. This was visually observed. Thus, close to this point the densities will be very similar, enabling very easy dispersion of the fluids, which may be beneficial for transport but not for separation. However, separation can easily be improved by altering the conditions according to the phase diagrams. Also, for this composition, there was a mismatch between the observed phases and the predicted ones at a higher temperature. Two liquid phases were observed, while predictions indicate a single liquid phase. The spikes observed in the torque plots (Figures 11 and 12) originate from stopping and starting wheel rotation for observation of the phases. As seen, upon restarting rotation to the same velocity, the torque value reverts to the values before stopping the wheel.

In the plot for FS10, the pressure, temperature, and torque vs time (0.5 m/s wheel velocity), upon cooling from the L (predicted) or LL (experimental) regions to the three-phase GLL region, are given. To the left, the phase diagram for the fluid is provided with the location of experimental T−ρ values. The GLL and L (LL) phases are indicated.

3.5. Dispersion Stability of CO_2-Rich Crude Oil Systems. Studies on dispersion formation and separation were performed on fluid systems FS8, FS9, and FS10 under various T−P conditions and velocities (shear-forces), giving separation times for a range of phase combinations. As this study was an introductory study to investigate the possibility of utilizing the wheel flow loop to study CO_2−crude oil

https://dx.doi.org/10.1021/acs.energyfuels.0c00818
Energy Fuels XXXX, XXX, XXX−XXX

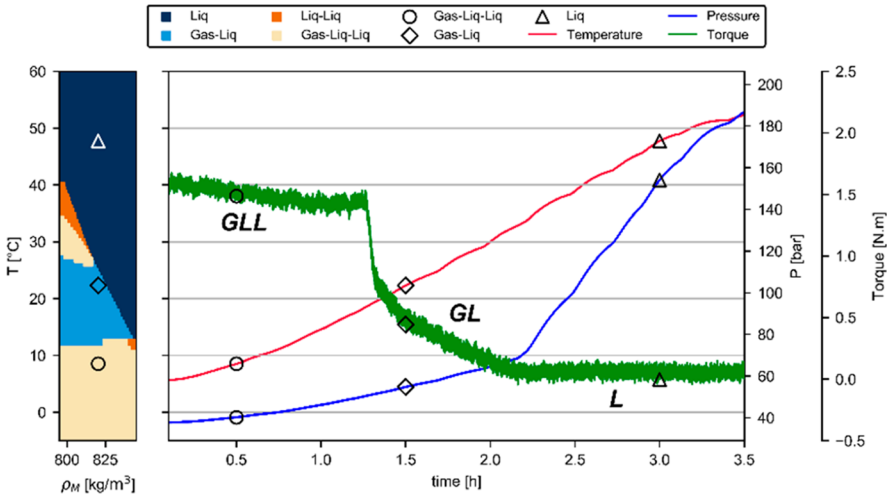

Figure 10. Results from phase transition values for FS9. Torque data (green line) dropped as temperature (red line) was increased, indicating phase transition. To the left is the phase diagram predicted for FS9. The wheel was rotated at 1.0 m/s while heating across the GLL/GL and GL/L phase boundary. Indicated on the plot are the GLL, GL, and L phases.

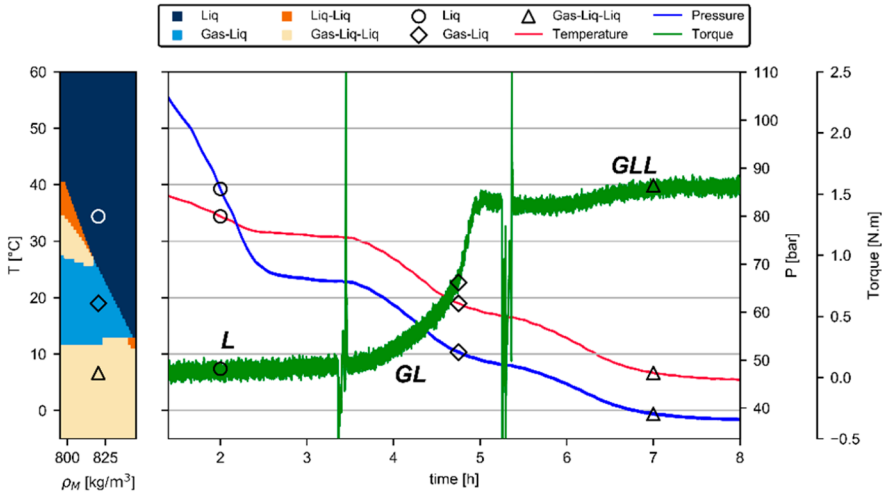

Figure 11. Results from phase transition data for FS9. Torque values (green line) increased as temperature (red line) was reduced, indicating phase transition. To the left is the phase diagram predicted for FS9. The wheel was rotated at 1.0 m/s while heating across the GLL/GL and GL/L phase boundary. Indicated on the plot are the GLL, GL, and the L phases.

dispersions, the number of different fluid system combinations and shear forces (rotational speed) were limited and not targeted to any particular field condition.

Table 4 provides tabulated results from the dispersion and separation studies on the various systems. The mixing velocity, given in meters per second, is an indication of the energy going into the formation of the dispersions. The rotational velocity was kept for around 2 min before stopping rotation and observing the $CO_{2(l)}$−oil interface and extract separation times from video recordings. For some systems, longer rotational times were tested without significant changes in the separation times. The average separation times were determined from several parallels giving a standard deviation for each separation time. Furthermore, the IFT values in Table 4 were evaluated from the previously described thermodynamic model combined with the linear gradient theory.[16,59]

Figure 13 shows pictures from the separation of oil in liquid CO_2 (CO_2 continuous) for FS8, illustrating the section of the wheel where the separation takes place for a given liquid fraction. Separation times for FS8 were on average 2.3 min when mixing with a velocity of 1.0 m/s. When increasing the energy input by increasing the rotational velocity to 2 m/s, the separation time increased to 3.1 min, indicating a strong effect of increased shear force. For FS8 under LL conditions, where the CO_2 was in a dense phase, the separation time was also 3.1 min after rotating at 2 m/s.

After adding more mineral oil to the system, achieving a CO_2/oil weight ratio of 1.1 compared to 2.1 for FS8, the system, when dispersed, became oil continuous for both FS9 and FS10. This may indicate the existence of an inversion point for liquid CO_2−crude oil dispersions, similarly to water−oil based dispersed systems where the relative amount of water (water cut) determines which phase is the continuous one. The effect of a lower CO_2/oil ratio was an increase in the separation time from 2.3 to 6.3 min under comparable conditions (row 1 vs row 4 in Table 4). The main reason for this increase is expected to be the difference in viscosity, as liquid CO_2 is considerably less viscous (approximately 0.06 mPa·s at around 27 °C and 80 bar[60]) than the liquid oil phases which were 1.7 and 5.0 mPa·s for the mineral oil and the crude

https://dx.doi.org/10.1021/acs.energyfuels.0c00818
Energy Fuels XXXX, XXX, XXX−XXX

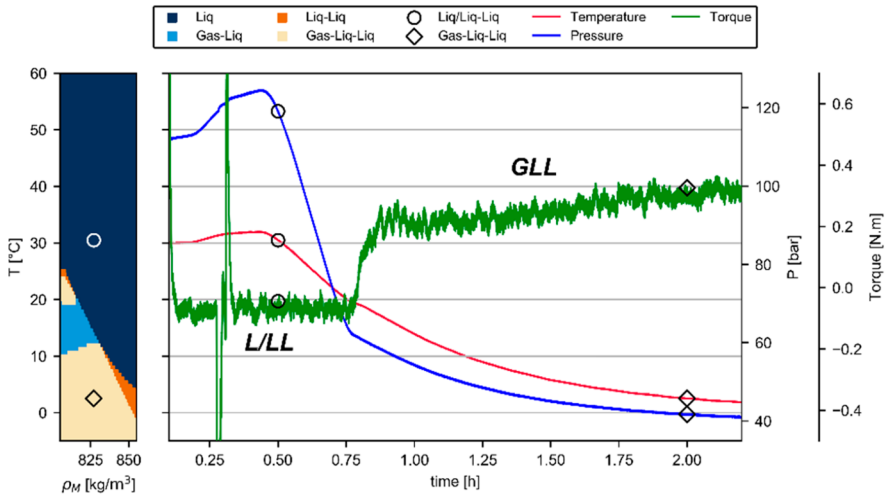

Figure 12. Results from phase transition data for FS10. Torque values (green line) increased as temperature (red line) was reduced, indicating phase transition. To the left is the phase diagram predicted for FS10. The wheel was rotated at 1.0 m/s while heating across the LL/GLL phase boundary. Indicated on the plot are the L/LL (observed was LL, predicted was L) and GLL phases.

Table 3. Summary of Experimentally Determined Phase Transition Temperatures and Pressures for FS7 to FS10

fluid system	transition type	temperature at phase transition [°C]	pressure at phase transition [bar]
FS7	GLL to LL	42.7 °C	84.5
FS8	GLL to LL	44.1 °C	87.0
FS9	GLL to GL	18.7 °C	50.6
FS9	GL to L (L)	32.7 °C	68.2
FS10	GLL to LL	19.5 °C	61.9

oil, respectively, under ambient conditions (Table 1). The viscosities for the oil system will probably be lower than the tabulated values for ambient conditions, due to CO_2 being dissolved in the oil phase but still considerably higher than the liquid CO_2 viscosity. For FS10, the separation time increased by 1.5 and 1.9 min for rotational speeds of 1 and 2 m/s, respectively, compared to FS9. Furthermore, the separation times for FS10 were not reduced considerably when reducing the mixing intensities from 2 to 1 m/s and to 0.5 m/s. Moreover, for both FS9 and FS10, the test temperature for the separation studies was 5 °C, while the pressures were 37 and 44 bar, respectively; thus both systems are in the GLL region of the phase diagrams (Figure 7).

3.6. Comparison of Experimental and Predicted Separation Times. With eq 1 above the separation time scales, τ_{corr} values were calculated for the cases in Table 4, taking into account the continuous phase viscosity, density difference, and the interfacial tension between the phases. The FS8 system had one condition (where the CO_2 was in the dense phase) with much higher density than the two other FS8

Table 4. Rotational Mixing Velocity of the Wheel, the Average Separation Times and the Standard Deviation for the Number of Parallel Separation Studies Included[a]

fluid system	mixing velocity [m/s]	average separation time [min]	standard deviation [min] (parallells)	density differences liquid CO_2 and oil [kg/m3]	IFT [mN/m]
FS8/GLL - oil/ CO_2(l)	1.0	2.3	0.3 (4)	79.6	0.59
FS8/LL - oil/ CO_2(dp)	2.0	3.1	0.1 (2)	237.5	2.22
FS8/GLL - oil/ CO_2(l)	2.0	3.1	0.1 (4)	79.6	0.59
FS9/GLL - CO2(l)/ oil	1.0	6.3	0.3 (5)	17.2	0.46
FS9/GLL - CO_2(l)/ oil	0.5	5.6	0.2 (3)	17.2	0.46
FS9/GLL - CO_2(l)/ oil	0.25	4.7	– (1)	17.2	0.46
FS10/GLL - CO_2(l)/ oil	0.5	7.5	– (1)	30.2	0.36
FS10/GLL - CO_2(l)/ oil	1.0	7.8	0.3 (2)	30.2	0.36
FS10/GLL - CO_2(l)/ oil	2.0	7.9	0.1 (2)	30.2	0.36

[a]Oil/CO_2 is a CO_2 continuous system and CO_2/oil is an oil continuous fluid system. For systems with only one test, a – is given instead of the standard deviation.

https://dx.doi.org/10.1021/acs.energyfuels.0c00818
Energy Fuels XXXX, XXX, XXX−XXX

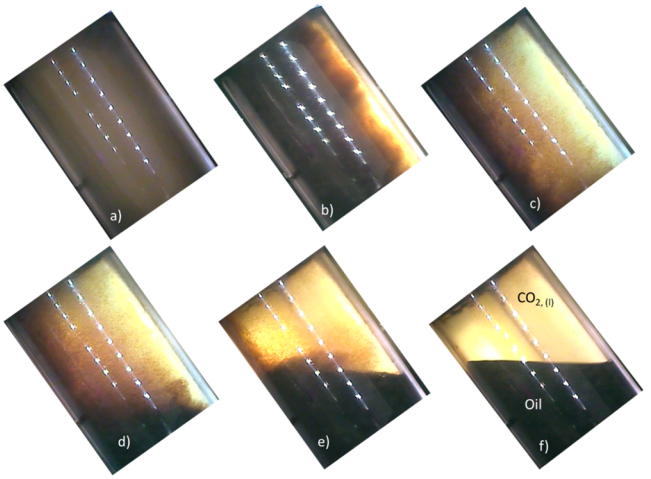

Figure 13. Pictures taken during separation of the CO_2−oil dispersion. (a) Dispersion before separation, (b) 15 s after shut-in, (c) 60 s after shut-in, (d) 105 s after shut-in, (e) 135 s after shut-in, and (f) 150 s after shut-in. The pictures are tilted so that they indicate the actual orientation of the window, showing the horizontal interface between the CO_2 and the oil, indicated in part f.

systems (237.5 vs 79.6 kg/m^3), while for FS9 and FS10, the T−P conditions, and thus density and viscosities, were the same. Furthermore, the IFT values were very low for all cases although slightly higher for the dense CO_2 phase condition of FS8, as expected.[59] Each fluid system had a nearly constant Eötvös number (Eo_p, FS8 (~3000), FS9 (~900), and FS10 (~2000)), calculated by using the inner diameter of the pipe (d_{pipe}) as the characteristic length scale, since the large scale interfaces at which drops can coalesce can be assumed to be approximately equal to the pipe diameter. The increase of Eo_p from FS9 to FS10 correlated with the increased separation times, and the Eo_p for the FS8 conditions varied by less than 10%, thus other factors such as viscosity and stabilization mechanisms or film drainage may explain the increased separation times when moving from FS8 to FS9 and FS10 (oil continuous systems).

To account for the viscosity, eq 1 as described above was developed for estimation of separation times (τ_{corr}). The tuning parameters obtained with the present data set were fitted such that κ_0 = 0.1 [min], κ_1 = 0.65, and κ_2 = 0.5. The experimental data were reasonably represented (within ±20%) of the predicted separation times, taking into account only the viscosity ratio and the Eötvös number (Figure 14). The higher viscosity of FS9 and 10 explains the increased separation times. Furthermore, as explained by Basheva et al.,[53] analyzing the coalescence of drops at a flat interface, a larger pushing force due to buoyancy also creates larger drop deformations which may slow down the film drainage process, inducing a larger rest time at the interface.

As observed from the measured data in Table 4, changes in separation times were also observed due to different rotational velocities giving different shear rates, which will produce different droplet size distributions.

The predicted d_{32} drop sizes fell in the range of ~0.2−2.3 mm for the experimental conditions. By utilizing the above-mentioned d_{32} values, Eötvös numbers $Eo_d = |\Delta\rho|gd_{32}/\sigma$ in the range of 0.1−2 were obtained.

In the expression above for τ_s, eq 2, by use of L_c, eq 3, and the expression for τ_c, eq 6, the constants $\{C_0, C_1, C_2\}$ and $\{\chi_0, \chi_1, \chi_2, \chi_3\}$ respectively, were jointly determined from the experimental data by minimizing the error on the overall separation time scale ($\tau_s + \tau_c$). A Particle Swarm Algorithm, described in Kennedy and Eberhart,[61] was used to aid the optimization procedure. The algorithm seeks to minimize a given function, here an RMS (root-mean-square) error measure between the experimental data and the correlation estimations for the separation time) in a chosen parametric space. The best fit for the length scale L_c (to determine τ_s), resulted in the following constants; C_0 = 0.29 [m], C_1 = 1.5, and C_2 = 1.5. For τ_c, the optimized constants were χ_0 = 0.407 [min], χ_1 = 0.64, χ_2 = 0.54, and χ_3 = 0.25.

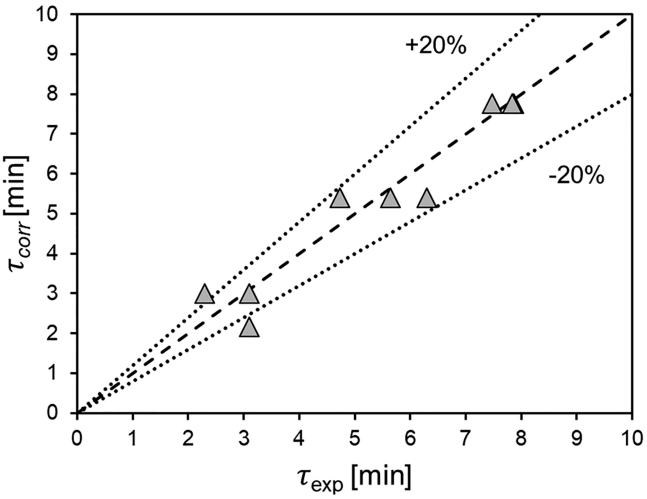

Figure 14. Comparison of predicted values by the simplified correlation.

Figure 15 depicts the ratio of the sedimentation time scale to the total measured separation time, as a function of the Eötvös number (defined with the drop diameter as length scale) showing how the data points collapse with a quite remarkable fit, indicating that the expressions for the time scales allow some representation of the experimental data. Furthermore, for the oil-in-CO_2 dispersion (FS8), the sedimentation time scale represented only less than 10% of the overall separation time, while for FS9 and FS10 the sedimentation time scale was on the same order as the separation time for very small Eo_d.

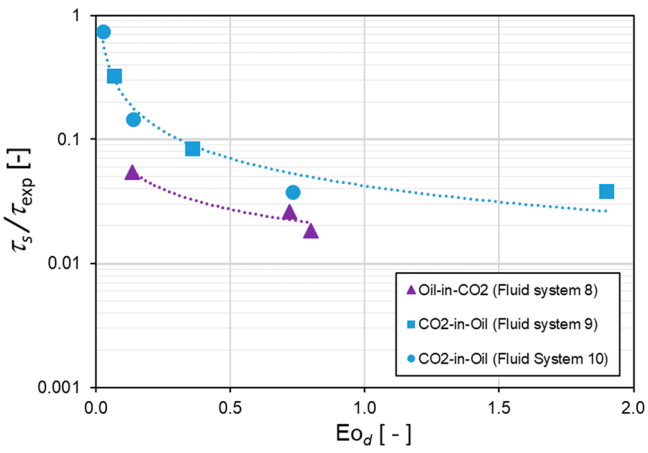

Figure 15. Ratio of the sedimentation time scale to the total measured separation time τ_s/τ_{exp} as a function of the Eötvös number Eo_d.

https://dx.doi.org/10.1021/acs.energyfuels.0c00818
Energy Fuels XXXX, XXX, XXX−XXX

A similar representation was done by plotting the ratio of the settling to measured time scales (τ_s/τ_{exp}) and coalescence to measured time scales (τ_c/τ_{exp}) respectively with the Weber number, where smaller droplets give a higher We and slower settling. The plots are shown below for FS8 (Figure 16) and

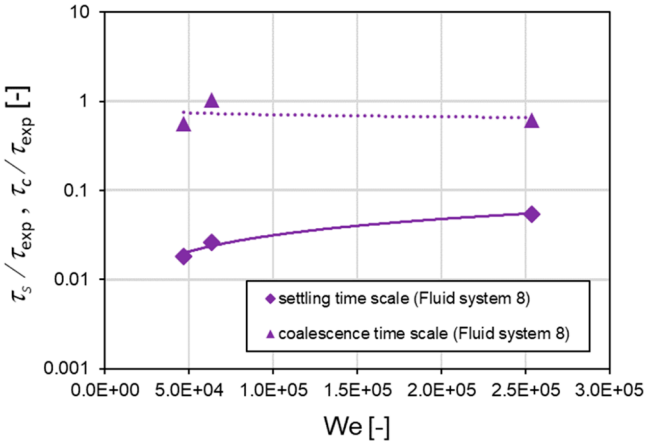

Figure 16. Ratio of the sedimentation and coalescence time scales to the total measured separation time τ_{exp} as a function of the Weber number We for FS8.

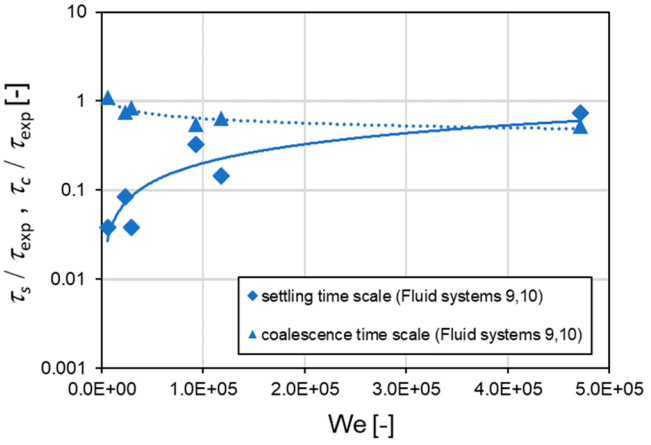

Figure 17. Ratio of the sedimentation and coalescence time scales to the total measured separation time τ_{exp} as a function of the Weber number We for FS9 and FS10.

FS9 and FS10 (Figure 17). For FS8, the coalescence time scale appeared to dominate the overall separation time despite the fast settling of the droplets due to the lower viscosity of CO_2. However, for FS9 and 10, upon increasing We numbers (giving smaller droplets due to higher wheel rotational velocities and thus shear rates), a decrease in the coalescence time scale was estimated on the same order of magnitude as the sedimentation time scale (the τ_s/τ_{exp} and τ_c/τ_{exp} curves approach each other). As a conclusion, the present interpretation suggests that at a low We (i.e., low rotational velocities/large droplet sizes), fast sedimentation occurred, and the separation process was limited by coalescence. For a high We (high rotational velocities/small droplet sizes), the results indicated that both sedimentation and coalescence processes were equally important.

4. CONCLUSIONS

SINTEF's wheel flow loop was used to obtain experimental data on phase properties such as volume fractions of phases present under given conditions and the temperature and pressure at which phase transitions occurred for the relevant fluid systems. The experimental values were compared with predicted phase diagrams from a Cubic Plus Associating (CPA) equation of state with Multiflash for the relevant compositions. The fluid systems tested ranged from pure CO_2 to CO_2 mixed with mineral oil, mineral oil/crude oil mixture, and a small amount (1 wt %) of methane. For the fluid systems containing only CO_2 and mineral oil, only two phases were obtained, namely, gas−liquid below and liquid−liquid above the critical point of the CO_2. When mixing in crude oil, three phases (GLL) were observed below the critical point and two phases above (LL) for FS7 and FS8. Increasing the oil/CO_2 ratio further led to the observation of three different phase regions, namely, GLL, GL, and LL. The addition of methane (FS10) had a large effect on the phase diagram and the phase transition points.

Experimental data on separation time scales were obtained and compared with models describing the separation. To model the separation, time scales were divided into a sedimentation and a coalescence part, which were calculated with the aid of a particle swarm algorithm using the experimental data to optimize the determination of the unknown constants in the equations. The predicted separation times of the model were comparable to the experimental data. Furthermore, the present interpretation of the separation studies suggested the following:

- For low Weber numbers, sedimentation was fast and the separation process was limited by coalescence.
- For high Weber numbers, both sedimentation and coalescence processes were indicated to be equally important.
- For the relevant fluid systems and similar fluid systems, the continuous phase will to a large degree govern the kinetics of separation meaning that CO_2 dispersed in oil will normally have a lower settling (or rising) rate than oil dispersed in a liquid CO_2 phase.

An additional observation, which should be pursued in further research, was the indication of possible inversion points for liquid CO_2−crude oil dispersions. Thus, the results obtained show that for separation and transport of CO_2 rich oil systems, knowledge of the dispersion and phase fraction properties is important in order to predict possible flow assurance and separation issues and opportunities. Furthermore, with the increasing focus on EOR with CO_2 such studies should be performed for the expected conditions for a given field over its lifetime, for both new and mature fields. Moreover, the possibility to monitor the torque when rotating the wheel at a constant velocity was shown to be useful to determine the point of phase transition. In such a context, the wheel flow loop approach is a highly relevant method for combined understanding of the thermodynamics and the dispersion properties of a given fluid system. For example, for a long pipeline where the pressure and temperature changes considerably, the wheel can be used to mimic both the temperature and pressure profiles as well as the duration of the transport of such fluid systems. This is not possible with a typical flow loop running with recirculation of the fluids by a separator.

https://dx.doi.org/10.1021/acs.energyfuels.0c00818
Energy Fuels XXXX, XXX, XXX−XXX

AUTHOR INFORMATION

Corresponding Author

Martin Fossen − *SINTEF AS, Multiphase Flow Laboratory, 7092 Tiller, Norway;* orcid.org/0000-0002-4612-0679; Email: martin.fossen@sintef.no

Authors

Marcelo A. Pasqualette − *ISDB Flowtech, 20040-004 Rio de Janeiro, Brazil;* orcid.org/0000-0002-6225-0473

João N. E. Carneiro − *ISDB Flowtech, 20040-004 Rio de Janeiro, Brazil*

Complete contact information is available at: https://pubs.acs.org/10.1021/acs.energyfuels.0c00818

Author Contributions

§These authors contributed equally. The manuscript was written through contributions of all authors. All authors have given approval to the final version of the manuscript.

Funding

Parts of this work were funded by the Research Council of Norway through the Basic Funding (Basisbevilgning, project no. 194070).

Notes

The authors declare no competing financial interest.

ACKNOWLEDGMENTS

We would like to acknowledge the Research Council of Norway, through the Basic Funding (Basisbevilgning, project no. 194070), for funding parts of this project. We thank Ivar Eskerud Smith for helping with the toroid volume calculations and Andrea Shmueli and Grethe Tangen for valuable inputs.

REFERENCES

(1) Middleton, R. S.; Keating, G. N.; Viswanathan, H. S.; Stauffer, P. H.; Pawar, R. J. Effects of Geologic Reservoir Uncertainty on CO2 Transport and Storage Infrastructure. *Int. J. Greenhouse Gas Control* **2012**, *8*, 132−142.

(2) Jarrell, P. M.; Fox, C.; Stein, M.; Webb, S. *Practical Aspects of CO2 Flooding*; SPE Monograph Series; Vol. *22*.

(3) Beltrao, R. L. C.; Sombra, C. L.; Lage, A. C. V. M.; Netto, J. R. F.; Henriques, C. C. D. SS: Pre-Salt Santos Basin - Challenges and New Technologies for the Development of the Pre-Salt Cluster, Santos Basin, Brazil. In *OTC-19880-MS*; Offshore Technology Conference, 2009; p 11. DOI: 10.4043/19880-MS.

(4) Almeida, A. S.; Lima, S. T. C.; Rocha, P. S.; Andrade, A. M. T.; Branco, C. C. M.; Pinto, A. C. C. CCGS Opportunities in the Santos Basin Pre-Salt Development. In *SPE International Conference on Health, Safety and Environment in Oil and Gas Exploration and Production, 12-14 April, Rio de Janeiro, Brazil*; Society of Petroleum Engineers, 2010.

(5) Blann, J. R.; Laville, G. M. Gas Lifting a Major oil Field in Argentina With High CO2 Content Associated Gas. *SPE Prod. Facil.* **1997**, *12* (01), 41−45.

(6) Crotti, M. A.; Fernandez, G. J.; Terrado, R. M. Improving Reserves and Production Using a CO2 Fluid Model in El Trapial Field, Argentina. In *SPE-107732-MS*; Society of Petroleum Engineers, 2007; p 8. DOI: 10.2118/107732-MS.

(7) Naveiro, J. T.; Haimson, D. Sapinhoá Field, Santos Basin Pre-Salt: From Conceptual Design to Project Execution and Results. In *OTC-26320-MS*; Offshore Technology Conference, 2015; p 19. DOI: 10.4043/26320-MS.

(8) Bo, W.; Castro, F.; Deplante, C.; Katekawa, M.; Balint, S. HSE in Libra Project − Designing for Outstanding Performance. In *OTC-28208-MS*; Offshore Technology Conference, 2017; p 8. DOI: 10.4043/28208-MS.

(9) Gaffney, C. *Review and Evaluation of Ten Selected Discoveries and Prospects in the Pre-Salt Play of the Deepwater Santos Basin, Brazil*; Technical Report to the Brazilian National Petroleum Agency (ANP): Brazil, 2010.

(10) Carvalhal, A. S.; Nunes Costa, G. M.; Vieira de Melo, S. A. B. Simulation of Enhanced oil Recovery in Pre-Salt Reservoirs: The Effect of High CO2 Content on Low Salinity Water Alternating Gas Injection. In *SPE-196684-MS*; Society of Petroleum Engineers: Abu Dhabi, UAE, 2019; p 11. DOI: 10.2118/196684-MS.

(11) Chapoy, A.; Burgass, R.; Tohidi, B.; Alsiyabi, I. Hydrate and Phase Behavior Modeling in CO2-Rich Pipelines. *J. Chem. Eng. Data* **2015**, *60* (2), 447−453.

(12) Al Ghafri, S. Z.; Maitland, G. C.; Trusler, J. P. M. Experimental and Modeling Study of the Phase Behavior of Synthetic Crude oil +CO2. *Fluid Phase Equilib.* **2014**, *365*, 20−40.

(13) Carneiro, J. N. E.; Pasqualette, M. A.; Reyes, J. F. R.; Krogh, E.; Johansen, S. T.; Ciambelli, J. R. P.; Rodrigues, H. T.; Fonseca, R. Numerical Simulations of High CO2 Content Flows in Production Wells, Flowlines and Risers. In *OTC-26231-MS*; Offshore Technology Conference, 2015; p 12. DOI: 10.4043/26231-MS.

(14) Pasqualette, M. A.; Rempto, M. J.; Carneiro, J. N. E.; Fonseca, R.; Ciambelli, J. R. P.; Johansen, S. T.; Løvfall, B. T. Parametric Study of the Influence of GOR and CO2 Content on the Simulation of a Pre-Salt Field Configuration. In *OTC-28093-MS*; Offshore Technology Conference, 2017; p 12. DOI: 10.4043/28093-MS.

(15) Rempto, M. J.; Pasqualette, M. A.; Fontalvo, E. M. G.; Carneiro, J. N. E.; Fonseca, R.; Ciambelli, J. R. P.; Johansen, S. T.; Løvfall, B. T. High CO2 Content Effect on the Flow of Crude oils in Production Transient Operations. In *BHR-2018−297*; BHR Group, 2018; p 15.

(16) Pasqualette, M. A.; Carneiro, J. N. E.; Johansen, S. T.; Løvfall, B. T.; Fonseca, R., Jr.; Ciambelli, J. R. P. A Numerical Assessment of Carbon-Dioxide-Rich Two-Phase Flows with Dense Phases in Offshore Production Pipelines. *SPE J.* **2020**, *25*, 0712.

(17) Sun, G.; Li, C.; Yang, S.; Yang, F.; Chen, Y. Experimental Investigation of the Rheological Properties of a Typical Waxy Crude oil Treated with Supercritical CO2 and the Stability Change in Its Emulsion. *Energy Fuels* **2019**, *33* (6), 4731−4739.

(18) Liu, Z. M.; Yang, G. Y.; Lu, Y.; Han, B. X.; Yan, H. K. Phase Equilibria of the CO2−Jiangsu Crude oil System and Precipitation of Heavy Components Induced by Supercritical CO2. *J. Supercrit. Fluids* **1999**, *16* (1), 27−31.

(19) Song, F. A Comprehensive Model for Predicting CO 2 Corrosion Rate in oil and Gas Production and Transportation Systems. *Electrochim. Acta* **2010**, *55*, 689−700.

(20) Rubin, A.; Wang, C. Qualification of Flexible Dynamic Risers for Supercritical CO2. In *OTC-23339-MS*; Offshore Technology Conference, 2012; p 10. DOI: 10.4043/23339-MS.

(21) Peng, C.; Crawshaw, J. P.; Maitland, G. C.; Trusler, J. P. M. Kinetics of Calcite Dissolution in CO2-Saturated Water at Temperatures between (323 and 373)K and Pressures up to 13.8 MPa. *Chem. Geol.* **2015**, *403*, 74−85.

(22) Mchugh, M. A.; Krukonis, V. J. *Supercritical Fluid Extraction*; Elsevier, 1994.

(23) Sandoval, G. A. B.; Soares, E. J.; Thompson, R. L.; Siqueira, R. do N.; de Andrade, R. M.; Campos, F.; Teixeira, A. Analysis of CO2 Hydrates in Crude oils from a Rheological Point of View. *Energy Fuels* **2018**, *32* (3), 2733−2741.

(24) de Souza, A. F. F.; Secchi, A. R.; de Souza, M. B. CO2 Subsea Separation: Concept & Control Strategies. *IFAC-PapersOnLine* **2019**, *52* (1), 790−795.

(25) Menezes, P.; Moura, D. A. G.; Marcos, F. B. A.; Pereira, S. J.; Mello, V. A. J.; Alves, F. L. F. HISEP: A Game Changer to Boost the oil Production of High GOR and High CO2 Content Reservoirs. In *OTC-29762-MS*; Offshore Technology Conference, 2019; p 5. DOI: 10.4043/29762-MS.

(26) Turek, E. A.; Metcalfe, R. S.; Fishback, R. E. Phase Behavior of Several CO2/ West Texas-Reservoir-oil Systems. *SPE Reservoir Eng.* **1988**, *3* (02), 505−516.

(27) Lucas, M. A.; Borges, G. R.; da Rocha, I. C. C.; Santos, A. F.; Franceschi, E.; Dariva, C. Use of Real Crude oil Fractions to Describe the High Pressure Phase Behavior of Crude oil in Carbon Dioxide. *J. Supercrit. Fluids* **2016**, *118*, 140−147.
(28) Alzobaidi, S.; Lee, J.; Jiries, S.; Da, C.; Harris, J.; Keene, K.; Rodriguez, G.; Beckman, E.; Perry, R.; Johnston, K. P.; Enick, R. Carbon Dioxide-in-oil Emulsions Stabilized with Silicone-Alkyl Surfactants for Waterless Hydraulic Fracturing. *J. Colloid Interface Sci.* **2018**, *526*, 253−267.
(29) Johnsen, E. E.; Førdedal, H.; Urdahl, O. A Simplified Experimental Approach for Measuring Viscosity for Water-in-Crude-oil Emulsions Under Flowing Conditions. *J. Dispersion Sci. Technol.* **2001**, *22* (1), 33−39.
(30) Schümann, H.; Fossen, M. oil-Water Dispersion Formation, Development and Stability Studied in a Wheel-Shaped Flow Loop. *J. Pet. Sci. Eng.* **2018**, *162*, 567−576.
(31) Johnsen, E. E.; Rønningsen, H. P. Viscosity of 'Live' Water-in-Crude-oil Emulsions: Experimental Work and Validation of Correlations. *J. Pet. Sci. Eng.* **2003**, *38* (1), 23−36.
(32) Urdahl, O.; Fredheim, A. O.; Løken, K.-P. Viscosity Measurements of Water-in-Crude-oil Emulsions under Flowing Conditions: A Theoretical and Practical Approach. *Colloids Surf., A* **1997**, *123−124*, 623−634.
(33) White, D. A.; Bond, J. A. A Low Shear Rate Turbulent Flow Apparatus. *Appl. Sci. Res.* **1971**, *23* (1), 368−372.
(34) Wolden, M.; Lund, A.; Nita, O.; Makogon, T.; Argo, C. B.; Larsen, R. *Cold Flow Black oil Slurry Transport of Suspended Hydrate and Wax Solids*; Tapir Forlag: Trondheim, Norway, 2005; p 40002.
(35) Kontogeorgis, G. M.; Voutsas, E. C.; Yakoumis, I. V.; Tassios, D. P. An Equation of State for Associating Fluids. *Ind. Eng. Chem. Res.* **1996**, *35* (11), 4310−4318.
(36) Peng, D.-Y.; Robinson, D. B. A New Two-Constant Equation of State. *Ind. Eng. Chem. Fundam.* **1976**, *15* (1), 59−64.
(37) Soave, G. Equilibrium Constants from a Modified Redlich-Kwong Equation of State. *Chem. Eng. Sci.* **1972**, *27*, 1197−1203.
(38) Péneloux, A.; Rauzy, E.; Fréze, R. A Consistent Correction for Redlich-Kwong-Soave Volumes. *Fluid Phase Equilib.* **1982**, *8* (1), 7−23.
(39) Jindrová, T.; Mikyška, J.; Firoozabadi, A. Phase Behavior Modeling of Bitumen and Light Normal Alkanes and CO2 by PR-EOS and CPA-EOS. *Energy Fuels* **2016**, *30* (1), 515−525.
(40) Bjørner, M. G.; Kontogeorgis, G. M. Modeling Derivative Properties and Binary Mixtures with CO2 Using the CPA and the Quadrupolar CPA Equations of State. *Fluid Phase Equilib.* **2016**, *408*, 151−169.
(41) Bjørner, M. G.; Sin, G.; Kontogeorgis, G. M. Uncertainty Analysis of the CPA and a Quadrupolar CPA Equation of State − With Emphasis on CO2. *Fluid Phase Equilib.* **2016**, *414*, 29−47.
(42) Riazi, M. R. Characterization and Properties of Petroleum Fractions; *ASTM manual series MNL 50*; ASTM International, 2005.
(43) Pedersen, K. S.; Christensen, P. L.; Shaikh, J. A. *Phase Behavior of Petroleum Reservoir Fluids*, 2nd ed.; CRC Press: Boca Raton, FL, 2014.
(44) Pedersen, K. S.; Fredenslund, A.; Christensen, P. L.; Thomassen, P. Viscosity of Crude oils. *Chem. Eng. Sci.* **1984**, *39* (6), 1011−1016.
(45) Pedersen, K. S.; Fredenslund, A. An Improved Corresponding States Model for the Prediction of oil and Gas Viscosities and Thermal Conductivities. *Chem. Eng. Sci.* **1987**, *42* (1), 182−186.
(46) Li, S.; Liu, M.; Hanaor, D.; Gan, Y. Dynamics of Viscous Entrapped Saturated Zones in Partially Wetted Porous Media. *Transp. Porous Media* **2018**, *125* (2), 193−210.
(47) Calabrese, R. V.; Chang, T. P. K.; Dang, P. T. Drop Breakup in Turbulent Stirred-Tank Contactors. Part I: Effect of Dispersed-Phase Viscosity. *AIChE J.* **1986**, *32* (4), 657−666.
(48) Kumar, A.; Hartland, S. Gravity Settling in Liquid/Liquid Dispersions. *Can. J. Chem. Eng.* **1985**, *63* (3), 368−376.
(49) Lagisetty, J. S.; Das, P. K.; Kumar, R.; Gandhi, K. S. Breakage of Viscous and Non-Newtonian Drops in Stirred Dispersions. *Chem. Eng. Sci.* **1986**, *41* (1), 65−72.
(50) Kamp, J.; Villwock, J.; Kraume, M. Drop Coalescence in Technical Liquid/Liquid Applications: A Review on Experimental Techniques and Modeling Approaches. *Rev. Chem. Eng.* **2017**, *33* (1), 1.
(51) Charles, G. E.; Mason, S. G. The Coalescence of Liquid Drops with Flat Liquid/Liquid Interfaces. *J. Colloid Sci.* **1960**, *15* (3), 236−267.
(52) Kamp, J.; Kraume, M. From Single Drop Coalescence to Droplet Swarms − Scale-up Considering the Influence of Collision Velocity and Drop Size on Coalescence Probability. *Chem. Eng. Sci.* **2016**, *156*, 162−177.
(53) Basheva, E. S.; Gurkov, T. D.; Ivanov, I. B.; Bantchev, G. B.; Campbell, B.; Borwankar, R. P. Size Dependence of the Stability of Emulsion Drops Pressed against a Large Interface. *Langmuir* **1999**, *15* (20), 6764−6769.
(54) Hartland, S.; Jeelani, S. A. K. Choice of Model for Predicting the Dispersion Height in Liquid/Liquid Gravity Settlers from Batch Settling Data. *Chem. Eng. Sci.* **1987**, *42* (8), 1927−1938.
(55) Jeffreys, G. V.; Davies, G. A.; Pitt, K. Rate of Coalescence of the Dispersed Phase in a Laboratory Mixer Settler Unit: Part I. *AIChE J.* **1970**, *16* (5), 823−827.
(56) Jaradat, M.; Attarakih, M.; Steinmetz, T.; Bart, H.-J. LLECMOD: A Bivariate Population Balance Simulation Tool for Pulsed Liquid-Liquid Extraction Columns. *Open Chem. Eng. J.* **2012**, *6* (1), 8−31.
(57) Henschke, M. *Dimensionierung liegender Flüssig-flüssig-Abscheider anhand diskontinuierlicher Absetzversuche, Fortschritt- Berichte VDI*; VDI Verlag. Thes, Düsseldorf, 1995.
(58) Poling, B. E.; Prausnitz, J. M.; O'Connell, J. P. *The Properties of Gases and Liquids*, 5th ed.; McGraw-Hill: New York, 2001.
(59) Zuo, Y.-X.; Stenby, E. H. A Linear Gradient Theory Model for Calculating Interfacial Tensions of Mixtures. *J. Colloid Interface Sci.* **1996**, *182* (1), 126−132.
(60) van der Gulik, P. S. Viscosity of Carbon Dioxide in the Liquid Phase. *Phys. A* **1997**, *238* (1), 81−112.
(61) Kennedy, J.; Eberhart, R. Particle Swarm Optimization. In *Proceedings of ICNN'95 - International Conference on Neural Networks*; Institute of Electrical and Electronics Engineers, 1995; vol. *4*, pp 1942−1948. DOI: 10.1109/ICNN.1995.488968.

https://dx.doi.org/10.1021/acs.energyfuels.0c00818
Energy Fuels XXXX, XXX, XXX−XXX